

This is a repository copy of Off-axis RF-sputtered barium titanate thin films for next-generation electro-optic devices.

White Rose Research Online URL for this paper: https://eprints.whiterose.ac.uk/id/eprint/233221/

Version: Published Version

Article:

Sumon, M.S.I., Lazareno, K., Carpenter, D.A. et al. (11 more authors) (2025) Off-axis RF-sputtered barium titanate thin films for next-generation electro-optic devices. Journal of Physics: Materials, 8 (4). 045011. ISSN: 2515-7639

https://doi.org/10.1088/2515-7639/ae0ef0

Reuse

This article is distributed under the terms of the Creative Commons Attribution (CC BY) licence. This licence allows you to distribute, remix, tweak, and build upon the work, even commercially, as long as you credit the authors for the original work. More information and the full terms of the licence here: https://creativecommons.org/licenses/

Takedown

If you consider content in White Rose Research Online to be in breach of UK law, please notify us by emailing eprints@whiterose.ac.uk including the URL of the record and the reason for the withdrawal request.





PAPER • OPEN ACCESS

Off-axis RF-sputtered barium titanate thin films for next-generation electro-optic devices

To cite this article: Md Saiful Islam Sumon et al 2025 J. Phys. Mater. 8 045011

View the <u>article online</u> for updates and enhancements.

You may also like

- From wide to ultrawide-bandgap semiconductors for high power and high frequency electronic devices
 Kelly Woo, Zhengliang Bian, Maliha Noshin et al.
- Simple method to enhance the coupling of THz electromagnetic pulses to antiferromagnetic spins
 Lucas van Gerven, Vladislav Bilyk, Rik Abeln et al.
- Roadmap on commercialization of metal halide perovskite photovoltaics
 Shien-Ping Feng, Yuanhang Cheng, Hin-Lap Yip et al.



Journal of Physics: Materials



OPEN ACCESS

RECEIVED

28 April 2025

REVISED

6 September 2025

ACCEPTED FOR PUBLICATION

1 October 2025

PUBLISHED

13 October 2025

Original content from this work may be used under the terms of the Creative Commons Attribution 4.0 licence.

Any further distribution of this work must maintain attribution to the author(s) and the title of the work, journal citation and DOI.



PAPER

Off-axis RF-sputtered barium titanate thin films for next-generation electro-optic devices

Md Saiful Islam Sumon¹, Katelyn Lazareno², David A Carpenter¹, Arnob Ghosh¹, Shrivatch Sankar¹, Imad I Faruque³, Sarvagya Dwivedi⁴, Robert L Nelson⁵, Dean P Brown⁶, Vincent E Stenger⁷, Benjamin G Griffin⁵, Robert Bedford⁵, Fengyuan Yang² and Shamsul Arafin^{1,*}

- ¹ Department of Electrical and Computer Engineering, The Ohio State University, Columbus, OH 43210, United States of America
- Department of Physics, The Ohio State University, Columbus, OH 43210, United States of America
- School of Mathematical and Physical Science, University of Sheffield, S3 7RH Sheffield, United Kingdom
- ⁴ Kilby Labs, Texas Instruments, Dallas, TX 75243, United States of America
- Materials and Manufacturing Directorate, Air Force Research Laboratory, Wright-Patterson AFB, Dayton, OH 45433, United States of America
- ⁶ UES Inc., a BlueHalo Company, Dayton, OH 45432, United States of America
- SRICO Inc., Columbus, OH 43235, United States of America
- * Author to whom any correspondence should be addressed.

E-mail: arafin.1@osu.edu

Keywords: barium titanate thin films, electro-optic modulator, RF sputtering, Pockels effect, silicon photonics Supplementary material for this article is available online

Abstract

In this work, we report the growth of 300 nm c-axis oriented barium titanate (BTO) films on (001)-strontium titanate (STO) substrates via off-axis radio frequency (RF) sputtering. The as-grown films exhibit exceptional crystallinity, with a rocking curve full width at half maximum of $\sim 0.03^{\circ}$, and atomically smooth surface morphology with a root mean square roughness of 0.23 nm, ensuring minimal optical losses. Transmission ellipsometric characterization of the film reveals a record-high electro-optic (EO) coefficient, $r_{51} \sim 550$ pm V⁻¹ that exceeds by a factor of 3 compared to the previously reported values for RF-sputtered BTO. This high-quality, industry-compatible material paves the way for the development of efficient and compact EO modulators based on hybrid BTO-on-silicon waveguides.

1. Introduction

The demand for high-speed, energy-efficient, and integrable electro-optic (EO) devices has spurred extensive research into advanced materials [1-4]. Silicon photonics, while CMOS-compatible, relies on the plasma dispersion effect, which suffers from high insertion loss, limited modulation speed, and significant power consumption [5, 6]. To address these limitations, ferroelectric-based modulators have gained interest due to their superior EO properties. In particular, thin-film ferroelectric materials are attractive because they combine strong intrinsic functional properties—such as large spontaneous polarization, nonlinear optical response, and strong dielectric tunability—with the scalability required for integration into micro- and nanoscale devices. Beyond EO modulators, they enable a broad range of applications in non-volatile memories, tunable microwave devices, and multifunctional oxide electronics [7]. Importantly, their integration in thin-film form makes it possible to harness these properties at reduced size, weight, and power, enabling compact photonic and electronic systems [8]. Among these, thin-film lithium niobate-on-insulator modulators, inspired by bulk LN, have demonstrated >100 GHz bandwidths [9, 10] with an EO coefficient of \sim 30 pm V⁻¹ [11]. This progress has driven the exploration of materials with higher EO coefficients, such as lead zirconate titanate (PZT) [12], BTO [13-15]. Pockels-effect modulators offer a high EO coefficient for efficient low-voltage phase modulation and ultrafast picosecond response times, making them ideal for high-speed optical communication and low-power integrated photonics [16].

BTO has emerged as a highly promising candidate for next-generation high-density integrated EO devices, primarily due to its exceptionally high Pockels coefficient, which exceeds 1300 pm V^{-1} in bulk form

[13, 17]. Despite its promise, scalable, cost-effective growth of high-quality BTO thin films remains challenging. Conventional methods including molecular beam epitaxy (MBE) [15] and pulsed laser deposition (PLD) [18] achieve exceptional crystallinity and EO coefficients ~1000 pm V⁻¹ but are expensive and unsuitable for wafer-scale production [19]. To overcome these challenges, cost-effective and industry-compliant radio frequency (RF) sputtering techniques [20–22] are currently investigated for the scalable growth of high-quality BTO thin films. An optimized RF sputtering process provides precise control over stoichiometry, crystallinity comparable to MBE or PLD and scalability of grown films.

The growth of 300 nm c-axis-oriented ('c-cut') BTO films on STO (001) substrates using RF magnetron sputtering is reported in this experimental study. By optimizing deposition conditions and employing low-energy off-axis sputtering to minimize energetic bombardment, we achieve atomically smooth surface morphology and excellent material crystallinity, as evidenced by atomic force microscopy (AFM) and x-ray diffraction (XRD), respectively. EO characterization confirmed an r_{51} coefficient of \sim 550 pm V $^{-1}$, highlighting the strong Pockels effect in the sputtered BTO films. We also evaluated the feasibility of EO devices using the grown material, an essential step toward realizing low-size, weight, power, and cost (SWaP-C) EO modulators for diverse applications.

2. Material growth

Conventional on-axis RF-sputtering often leads to energetic ion bombardment due to a higher energy (E) of the emitted atoms, which degrades crystalline quality and introduces structural defects. To overcome this challenge, off-axis RF sputtering (see figure 1(a)) was employed in this study, which minimizes ion-induced damage due to lower E of the emitted atom while preserving the stoichiometric precision necessary for high-quality film growth with its crystallinity comparable to MBE and PLD. In our configuration, the target is mounted on a horizontally oriented sputtering source, and the substrate is positioned below the target facing upward. The horizontal distance between the target and the center of the substrate is 5.7 cm, while the vertical distance between the center of the target and the substrate is 7.6 cm, yielding a target-to-substrate distance of 9.5 cm and an off-axis angle of 53°. With this optimized off-axis geometry, 300 nm c-cut BTO thin films were deposited on STO (001), as schematically shown in figure 1(b), at a substrate temperature of 550 °C, under 10 mTorr Ar pressure with 0.125% O₂. The 300 nm thickness is selected to optimize high-quality growth, the primary objective of this work, using off-axis RF sputtering, and to provide a foundation for future thickness adjustments tailored to EO modulator designs. Given that BTO exhibits a tetragonal lattice structure at room temperature (a = b = 3.99 Å, c = 4.03 Å), epitaxial growth on STO (001) with its in-plane square lattice constant of 3.905 Å results in compressive strain within the BTO film. This strain forces c-axis orientation of the film normal to the growth surface. Figure 1(c) shows the optical micrograph of the films. AFM measurements were performed to examine the surface morphology of the films. The measured root mean square roughness over a 2.5 μ m \times 2.5 μ m BTO area was 0.23 nm, as presented in figure 1(d). This exceptionally smooth surface is crucial for reducing optical scattering and enhancing EO efficiency, making these films highly suitable for photonic and optoelectronic applications.

3. Material characterization

The BTO film growth conditions were systematically optimized by varying substrate temperature, RF-sputtering power, and oxygen partial pressure on STO(001) substrates. From this process, a growth temperature of 550 °C, RF power of 50 W, and oxygen partial pressure of 0.125% were identified as the most optimized parameters, yielding the best crystalline quality. All subsequent BTO films reported in this work were grown under these optimized conditions. To evaluate the structural characteristics, XRD measurements were performed using the θ -2 θ scan geometry. BTO films of varying thicknesses, such as 10 nm, 30 nm, 100 nm, and 300 nm were deposited on STO(001) substrates to study thickness-dependent crystallinity, as shown in figure 2(a). With increasing thickness, the c-BTO (001) diffraction peaks suggest that the grown films retain its crystallinity. Additionally, a clear peak shift to larger 2θ values is observed for thicker films, suggesting strain relaxation. The detailed calculation of the relaxation from the XRD data, including the quantitative values, is provided in the supplementary section S1. To directly probe the in-plane lattice parameter and confirm this relaxation, reciprocal space mapping (RSM) around the asymmetric (103) reflection was performed for the optimized 300 nm BTO film, as shown in figure 2(b). The map reveals two distinct diffraction peaks: a sharp, intense peak at higher q_z from the STO substrate, and a broader, lower-intensity peak at $q_x \approx 0.25 \text{ Å}^{-1}$ and $q_z \approx 0.74 \text{ Å}^{-1}$ from the BTO film. If the BTO film were fully strained to the substrate, its peak would align vertically with the STO peak along q_x , sharing the same in-plane lattice constant. Instead, the clear horizontal offset of the BTO peak indicates that the in-plane lattice constant has relaxed away from the substrate value toward the bulk BTO parameter. The peak position

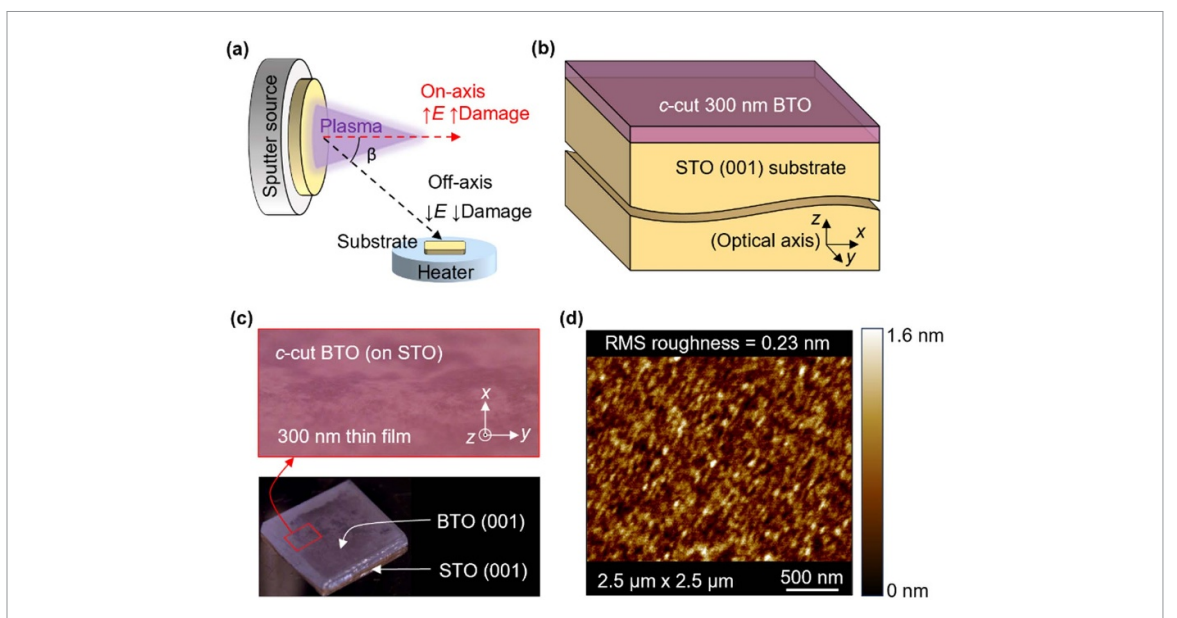


Figure 1. (a) Schematic of the RF-sputtering process, emphasizing off-axis deposition and its role in reducing energy-induced damage, (b) schematic of the grown structure, (c) optical microscope image, and (d) atomic force microscopy scan of the 300 nm c-cut BTO thin film on STO (001) substrates.

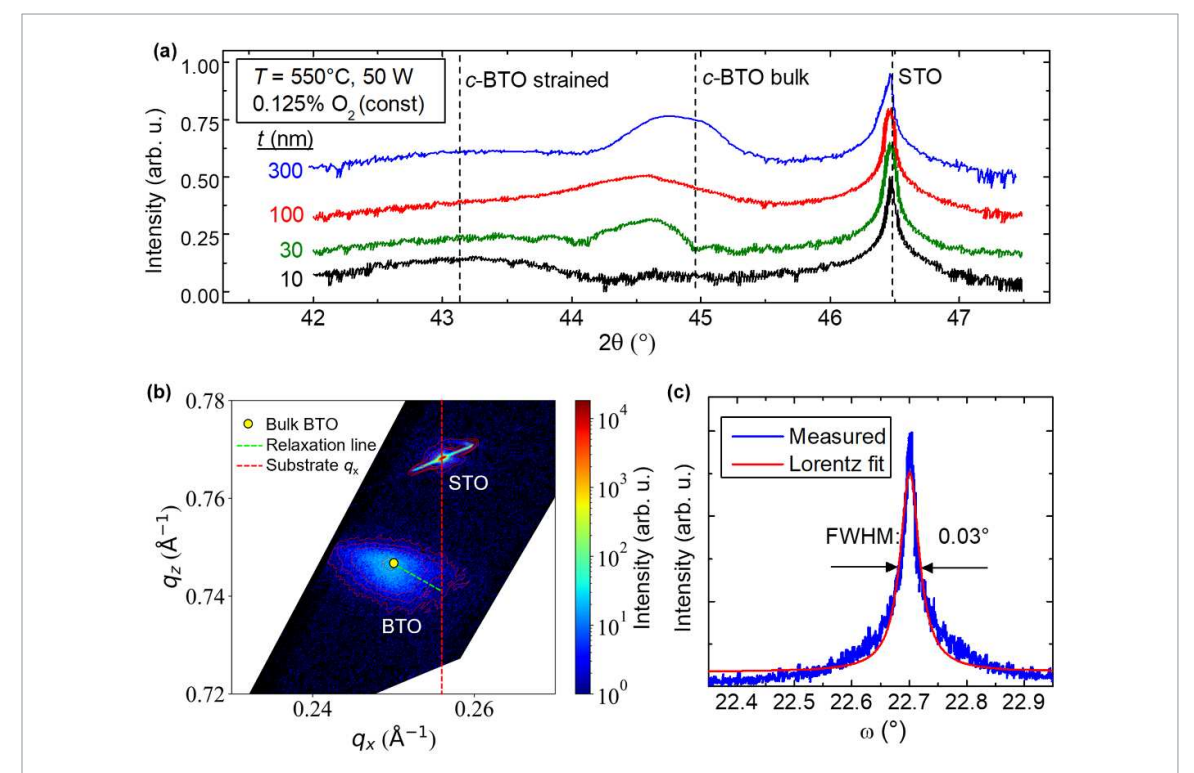


Figure 2. (a) XRD θ -2 θ scans of BTO films of varying thicknesses under the same oxygen partial pressures, substrate temperature, and RF-sputtering power, (b) RSM around the asymmetric (103) reflection for the 300 nm BTO film, confirming that the film is fully relaxed in-plane, and (c) XRD rocking curve of the 300 nm BTO (001) films.

confirms that the 300 nm BTO film is fully relaxed in-plane, while its broadening relative to the substrate reflects mosaicity and residual strain distribution, as expected for thicker epitaxial films undergoing relaxation. Together, the θ –2 θ strain analysis and the RSM provide complementary evidence that the 300 nm BTO film is essentially relaxed both out-of-plane and in-plane. Figure 2(c) presents the rocking curve of the (002) diffraction peak from the 300 nm-thick BTO film (corresponding to the blue curve in figure 2(a)), fitted with a Lorentzian function. The peak is centered at 22.7° with a full width at half maximum of 0.03°, indicating excellent crystallinity, low mosaicity, and a high degree of single-crystalline ordering. These results confirm that BTO films grown under optimized conditions maintain their structural quality even at increased thicknesses.

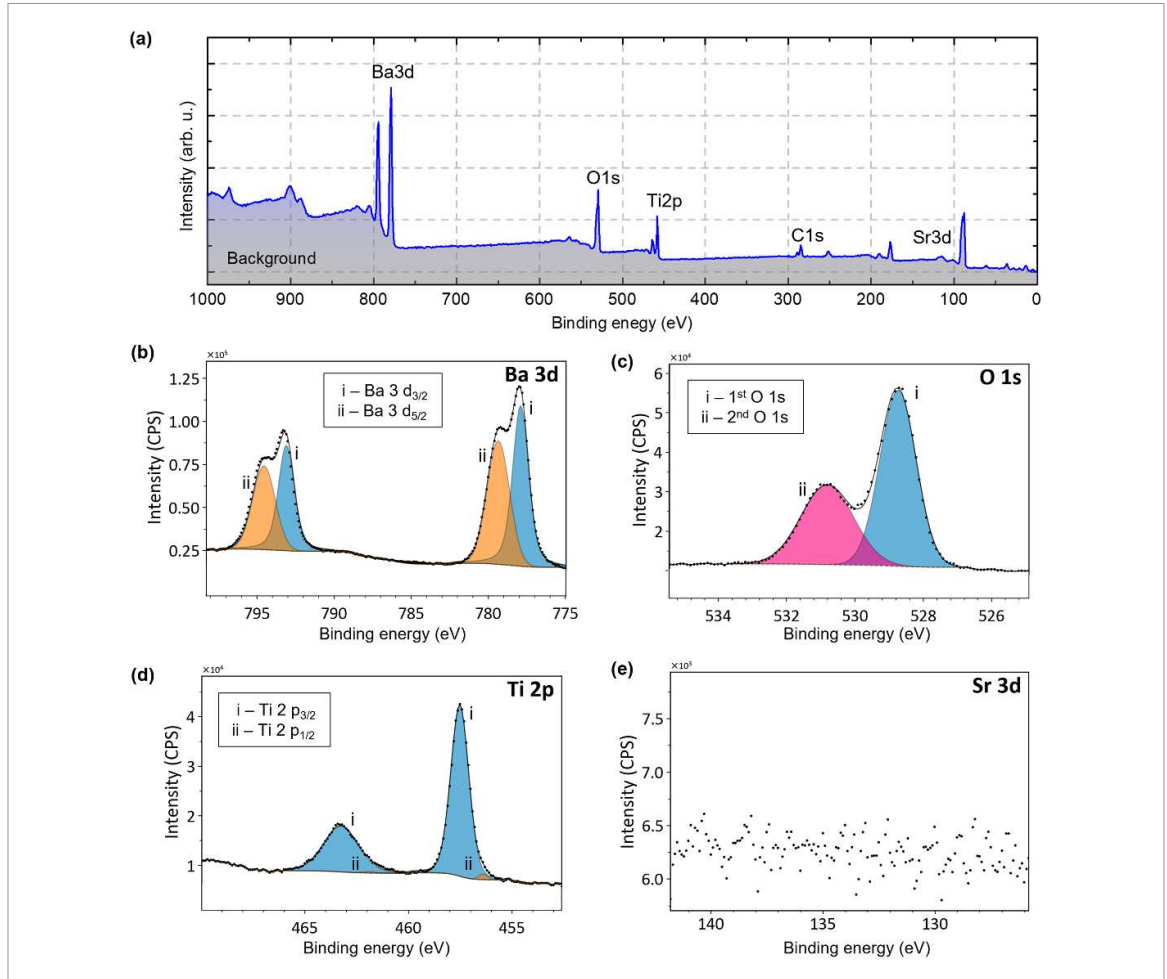


Figure 3. XPS spectra of BTO/STO: (a) survey, (b) Ba 3d, (c) O 1s, (d) Ti 2p, and (e) Sr 3d. Clear Ba, Ti, and O signals confirm the BTO film, while the absence of Sr 3d indicates full substrate coverage.

To complement the structural studies, x-ray photoelectron spectroscopy (XPS) was performed to investigate the elemental composition, chemical states, and defects of the optimized BTO films. XPS was performed for a 300 nm BTO thin film on STO, with survey spectra collected at 100 eV pass energy and high-resolution spectra at 20 eV pass energy. The resulting spectra were calibrated based on the C–C peak at 284.6 eV and fitted using Khervefitting software. The survey spectrum (figure 3(a)) shows the Ba 3d, O 1s, Ti 2p, C 1s, and Sr 3d regions, consistent with a clean perovskite-oxide surface.

The high-resolution Ba 3d spectra of the BTO films are shown in figure 2(b). Two overlapping spin–orbit-split doublets (i) and (ii) corresponding to Ba $3d_3/_2$ (i) and Ba $3d_5/_2$ (ii) are observed, separated by \sim 1.4 eV, with a spin–orbit splitting (Δ Ba 3d) of \sim 15.2 eV. These values are consistent with previously reported data [23–25]. The lower-binding-energy doublet (i) is assigned to barium in the perovskite BTO lattice [24–26]. In contrast, the higher-binding-energy doublet (ii) is attributed to surface barium species such as BaCO₃ or Ba(OH)₂ [23, 27].

The high-resolution O 1s spectrum of the thin BTO films is shown in figure 3(c). The deconvolution of the O 1s peaks for the BTO films yields two distinct components (i) and (ii), fitted using a Gaussian–Lorentzian function. These features are consistent with previous reports [28–31]. The higher-binding-energy peak (ii) is attributed to lattice oxygen in the perovskite BTO structure, specifically the Ti–O–Ti bonding environment [28, 32]. The lower-binding-energy peak (i) is likely associated with oxygen in the form of M–O–Ti bonds (M = metal) [28, 33]. Importantly, no additional high-binding-energy features were detected, which are typically associated with oxygen vacancies or surface adsorbates [28, 34].

The deconvolution of the high-resolution XPS spectrum of Ti 2p is shown in figure 2(d), exhibiting the characteristic spin—orbit doublet with the Ti $2p_3/_2$ component more intense than the Ti $2p_1/_2$ component, consistent with the expected 2:1 area ratio. The spin—orbit splitting (Δ Ti 2p) between Ti $2p_3/_2$ and Ti $2p_1/_2$ is \sim 5.73 eV in the BTO film. For these films, the spectra show two main peaks at i, in good agreement with previously reported binding energies of Ti⁴⁺ [28, 33]. Additionally, weak features at ii are attributed to Ti³⁺ states [28, 33]. The presence of negligible Ti³⁺ indicates negligible oxygen vacancies. This is consistent with

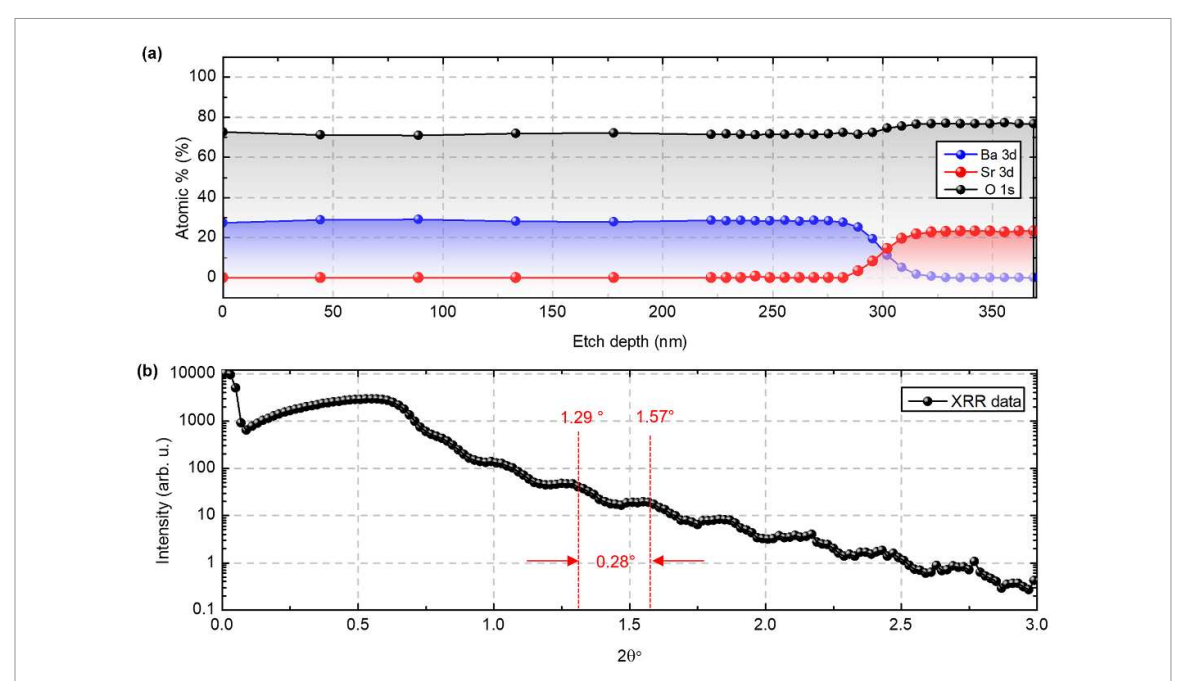


Figure 4. (a) XPS depth profile of BTO/STO showing strong Ba 3d and O 1s signals at the surface. With sputtering, the Sr 3d signal emerges while Ba 3d decreases, confirming the transition from the BTO film to the STO substrate near 300 nm, and (b) XRR scan of a \sim 30 nm BTO film on STO, showing Kiessig fringes used to determine thickness and calibrate the deposition rate.

the negligible oxygen vacancies coming from the O 1s spectrum, where the absence of higher-energy components confirmed negligible oxygen vacancies. This is particularly advantageous for our case, as excessive oxygen vacancies pin domain walls, suppress polarization, and reduce the dielectric constant. Moreover, vacancy-induced Ti³⁺ states absorb visible light, thereby increasing optical losses—detrimental to photonic and EO applications, such as modulators or frequency conversion devices. High vacancies also compromise the chemical stability of BTO, making it more prone to leakage currents.

The Sr 3d XPS region (126–142 eV) of figure 2(e) does not exhibit any discernible Sr-related peaks, indicating that the STO substrate signal is fully suppressed by the overlying BTO film. This absence of Sr signature is consistent with the surface sensitivity of XPS and confirms the continuous coverage of the STO substrate by the BTO layer.

Ar⁺ sputter depth profiling with XPS (figure 4(a)) further validates the film–substrate interface. A sharp Ba→Sr crossover is observed near 300 nm, while O 1s remains broadly constant with only a subtle kink across the interface. The delayed emergence of the Sr 3d signal until this depth indicates full film coverage without Sr enrichment at the outer surface. Although Ti 2p scans were not recorded during sputtering, the Ba 3d and Sr 3d profiles provide sufficient evidence of depth distribution and confirm the abrupt film–substrate interface. These results demonstrate both the chemical integrity of the BTO film and its sharp interface with the underlying STO substrate.

Furthermore, the film thickness was calibrated using x-ray reflectivity (XRR). For this purpose, a reference BTO film with a nominal thickness of \sim 30 nm was grown under the optimized conditions and analyzed by XRR, as shown in figure 4(b). The reflectivity profile exhibits clear Kiessig fringes, from which the film thickness was extracted to be \sim 31.6 nm. Using this calibration, the deposition rate was determined, and the thicknesses of the thicker films (100 nm and 300 nm) were subsequently obtained by multiplying the deposition rate by the deposition time. The detailed calculation is provided in supplementary section S2.

In addition to crystallinity, chemical composition, and thickness calibration, the role of defect formation—particularly oxygen vacancies, non-stoichiometry, and dislocation density—must also be considered, as these play a critical role in determining the ferroelectric and EO behavior of BTO thin films. Given that Ba²⁺ and Ti⁴⁺ BTO are the most stable oxidation states while sufficient oxygen is provided by the target and oxygen gas during sputtering, the oxygen vacancies in BTO should be minimal (which is the case for other oxides that we have grown by us, such as [35–39]). This is consistent with the negligible oxygen vacancy-related features in the XPS spectra (figure 3). Regarding dislocations, the XRD results indicate that the 30 nm BTO film is already largely relaxed (figure 2(b)), implying that strain relaxation—and the associated formation of dislocations—is mostly accommodated within the first 10–30 nm of growth. Consequently, the vast majority (>90%) of the 300-nm films used for EO measurements are bulk-like, with the influence of interfacial dislocations confined to a small fraction (~3%–10%) near the substrate.

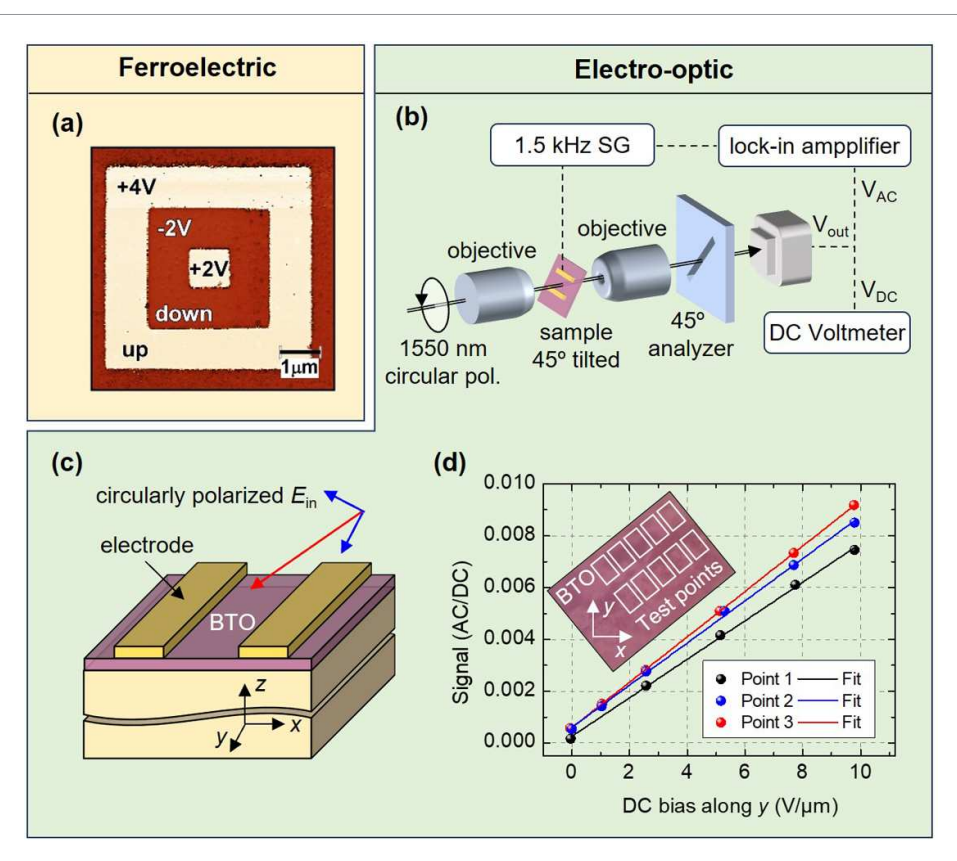


Figure 5. (a) Piezoresponse force microscopy (PFM) image of ferroelectric (FE) switching in a 10 nm BTO film on an SRO (10 nm)/DSO(110) substrate under applied biases, (b) schematic of the EO measurement setup used in the study, (c) schematics of patterned BTO films with gold electrodes for EO testing with polarization modulation along the *x*–*y* plane indicated by arrows, and (d) measured AC/DC EO response at three different test points on the BTO film, showing a linear electro-optic effect with a strong correlation between applied field and modulation signal. Top view of the sample with the tested regions (not to scale) is shown as inset.

4. Ferroelectric and EO characterization

The ferroelectric polarization and nonlinear optical response in BTO arise from the broken inversion symmetry in its tetragonal crystal lattice, making an understanding of its ferroelectric domain structure critical for optimizing integration into photonic devices. To investigate this, piezoresponse force microscopy (PFM) was employed to image and manipulate ferroelectric domains in the grown BTO films. The PFM image in figure 5(a) illustrates the ferroelectric switching behavior of BTO. For this test, a 10 nm-thick BTO layer was deposited on 10 nm of $SrRuO_3$ (SRO) on (110)-oriented $DyScO_3$ (DSO) substrate, which serves as a bottom electrode to facilitate ferroelectric switching. The XRD and AFM information of the sample used for PFM is added in the supplementary section S3. A sequence of +4 V, -2 V, and +2 V voltage biasing was applied to three concentric square regions of decreasing size to induce controlled polarization switching. The observed contrast in the image represents domains polarized 'up' (light regions) and 'down' (dark regions). The ability to reversibly switch ferroelectric domains with well-defined polarization boundaries confirms that the BTO epitaxial films are single-crystalline, and uniformly switchable. This uniform switching response, coupled with the high-quality epitaxial growth of BTO, ensures stable and reproducible ferroelectric polarization, which is essential for nonlinear optical applications and EO modulation.

The transmission ellipsometric measurement setup, shown in figure 5(b), comprised a signal generator (SG), a 100 kHz bandwidth photodiode (PD), a lock-in amplifier, and a DC voltmeter to analyze the modulation response. The SG applied an alternating voltage with a DC bias to the BTO thin-film modulator, triggering the EO effect. The lock-in amplifier enhances the signal-to-noise ratio by isolating the EO modulation signal from background interference, while the DC voltmeter provides the PD's DC offset relative to the strength of the laser coming through the measurement setup. The lock-in signal is relative to the optical intensity, the SG applied voltage, and the EO coefficient.

Year Thickness EO coefficient Substrate References $r_{42} \sim 27 \text{ pm V}^{-1}$ 2017 MBE STO + MBE BTO/Si96 nm [41] $r_{\rm eff} = 41 \; \rm pm \; V^{-1}$ $r_{\rm eff} = 6 \text{ pm V}^{-1}$ 2017 Si 102 nm [41] STO/SOI 2021 100-1000 nm $r_{\rm eff} = 157 \; \rm pm \; V^{-1}$ [21] $r_{33} > 130 \text{ pm V}^{-1}$ 2023 STO/SOI 100 nm [42] STO 300 nm $r_{51} \sim 550 \text{ pm V}^{-1}$ This work 2025

Table 1. RF-sputtered BTO thin films reported in literature.

In order to perform the transmission ellipsometric measurement, the 300 nm BTO film grown on dual-side polished STO substrates was then patterned with gold electrodes as schematically shown in figure 5(c). These electrodes facilitate the application of both DC and AC electric fields, inducing polarization modulation along the x-z plane of the film. The setup utilized circularly polarized input light at 1550 nm, focused through a 20 μ m gap between the objectives with an analyzer set at 45° relative to the direction of the applied field. DC and AC electric fields (1.5 kHz) were applied to modulate the EO response of the film. As supported by both experimental data and theoretical modeling, the EO modulation signal was absent at the fundamental SG frequency (1.5 kHz) unless a DC bias was applied, confirming the role of the applied field in enabling EO response. This configuration ensures that the EO effect is primarily influenced by the off-diagonal EO tensor component r_{51} , a key parameter for phase modulation in integrated photonic applications.

To evaluate the EO effect, modulation response measurements were conducted at several spatial locations of our large-area BTO films (figure 5(d)). The experimental results demonstrate a linear correlation between the applied electric field and the resulting modulation signal, indicating the presence of the linear EO (Pockels) effect in the material. This study presents a novel direct measurement of the EO coefficient r_{51} in our system—equivalent to r_{42} in the standard BTO crystallographic notation—yielding a value of approximately 550 pm V⁻¹ for 300 nm-thick BTO. While some insights into the measurement setup can be obtained from [40], the detailed derivation of the measurement technique, including the mathematical model and numerical analysis, shall be presented in a future publication. Using this approach, the EO response was found to be reproducible across multiple spatial locations on the same film, as demonstrated by measurements at three different sample positions of figure 3(d). In addition, repeatability tests performed at a fixed position over ten consecutive bias cycles showed no hysteresis, drift, or degradation. These additional results, included in the supplementary section S4, confirm that the r_{51} coefficient remains stable under repeated cycling. Based on the published data summarized in table 1, the measured EO-coefficient \sim 550 pm V⁻¹ in this work represents a significant advancement over previously reported RF-sputtered BTO thin films approaching the EO performance of bulk BTO materials.

5. Modulator design and future work

The large r_{51} EO coefficient achieved in off-axis RF-sputtered BTO motivates the development of photonic devices that leverage this strong 'off-diagonal' EO response. One such device concept, illustrated in figure 6(a), is a hybrid Si-on-BTO polarization mode modulator. In this design, 100 nm thick high-quality Si layer would be deposited via an appropriate deposition process onto the BTO surface, patterned to define the waveguide, and engineered to ensure strong optical confinement in BTO, as shown in figures 6(b) and (c).

A key challenge in this architecture is achieving phase matching between the fundamental transverse electric (TE) and transverse magnetic (TM) modes, which is essential for efficient EO polarization modulation. This can be addressed using two complementary strategies: (1) dispersion engineering, by precisely tuning the waveguide dimensions to align the phase velocities of the TE and TM modes [21], thereby optimizing their overlap with BTO's r_{51} coefficient; and (2) implementing a periodic interdigital electrode structure [43], which enables selective modulation of the effective refractive indices through controlled birefringence, facilitating quasi-phase matching for improved modulation efficiency.

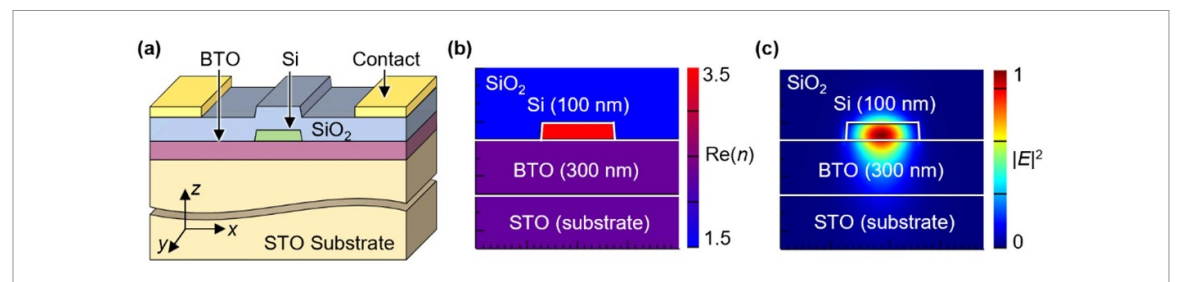


Figure 6. (a) Schematic of a hypothetical hybrid BTO-on-silicon modulator structure, where Si ridge guides the optical mode, and metal contacts on the SiO_2 buffer layer for electro-optic modulation. (b) Simulated refractive index n distribution and (c) electric field intensity ($|E|^2$) with a mode confinement in the hybrid BTO-Si waveguide.

6. Conclusion

This work positions RF-sputtered BTO thin films as a highly scalable platform suitable for compact, low-power EO devices, unlocking new possibilities for next-generation high-speed photonic and quantum technologies. Our optimized off-axis RF-sputtering process enabled the deposition of single-crystalline 300 nm BTO films with ultra-smooth surfaces. EO characterization confirmed a large r_{51} coefficient of \sim 550 pm V $^{-1}$, surpassing both lithium niobate and other RF-sputtered BTO demonstrations. Additionally, we demonstrated a method to integrate the grown material into Si-BTO hybrid waveguides for realizing a polarization mode converter leveraging r_{51} -based EO modulation. Future work will focus on device integration, including traveling-wave electrodes for high-speed operation and growth optimization of a-cut BTO. These findings pave the way for scalable, high-performance EO devices, advancing low-power, ultrafast photonic and quantum technologies.

Data availability statement

All data that support the findings of this study are included within the article (and any supplementary files).

Acknowledgment

The authors would like to thank Dr. Ricky Gibson for his valuable comments and insightful discussions, as well as the Surface Analysis Laboratory (SAL) at The Ohio State University.

Funding

Support for this effort was provided with seed funding from the OSU President's Research Excellence (PRE) Accelerator Program. This material is based on research sponsored by the Air Force Research Laboratory and Strategic Council for Higher Education under Agreement FA8650-19-2-9300. The U.S. Government is authorized to reproduce and distribute reprints for Governmental purposes notwithstanding any copyright notation thereon.

Conflict of interest

The authors declare no conflicts of interest.

ORCID iDs

Sarvagya Dwivedi © 0000-0003-1184-3225 Dean P Brown © 0009-0000-8058-1738 Fengyuan Yang © 0000-0001-6921-1533 Shamsul Arafin © 0000-0003-4689-2625

References

- [1] Liu J, Xu G, Liu F, Kityk I, Liu X and Zhen Z 2015 Recent advances in polymer electro-optic modulators RSC Adv. 5 15784-94
- [2] Sinatkas G, Christopoulos T, Tsilipakos O and Kriezis E E 2021 Electro-optic modulation in integrated photonics J. Appl. Phys. 130 010901

- [3] Ma Z, Li Z, Liu K, Ye C and Sorger V J 2015 Indium-tin-oxide for high-performance electro-optic modulation Nanophotonics 4 198–213
- [4] Jin M, Wei Z, Meng Y, Shu H, Tao Y, Bai B and Wang X 2022 Silicon-based graphene electro-optical modulators Photonics 9 82
- [5] Han C, Jin M, Tao Y, Shen B and Wang X 2022 Recent progress in silicon-based slow-light electro-optic modulators Micromachines 13 400
- [6] Shekhar S, Bogaerts W, Chrostowski L, Bowers J E, Hochberg M, Soref R and Shastri B J 2024 Roadmapping the next generation of silicon photonics Nat. Commun. 15 751
- [7] Ramesh R and Spaldin N A 2007 Multiferroics: progress and prospects in thin films Nat. Mater. 6 21-29
- [8] Hu Y et al 2025 Integrated lithium niobate photonic computing circuit based on efficient and high-speed electro-optic conversion Nat. Commun. 16 8178
- [9] Weigel P O et al 2018 Bonded thin film lithium niobate modulator on a silicon photonics platform exceeding 100 GHz 3-dB electrical modulation bandwidth Opt. Express 26 23728–39
- [10] He M et al 2019 High-performance hybrid silicon and lithium niobate Mach–Zehnder modulators for 100 Gbit/s and beyond Nat. Photon. 13 359–64
- [11] Weis R S and Gaylord T K 1985 Lithium niobate: summary of physical properties and crystal structure Appl. Phys. A 37 191-203
- [12] Alexander K, George J P, Verbist J, Neyts K, Kuyken B, Van Thourhout D and Beeckman J 2018 Nanophotonic Pockels modulators on a silicon nitride platform Nat. Commun. 9 3444
- [13] Boyd R W, Gaeta A L and Giese E 2008 Nonlinear optics Springer Handbook of Atomic, Molecular, and Optical Physics (Springer) pp 1097–110
- [14] Eltes F, Li W, Berikaa E, Alam M S, Bernal S, Minkenberg C, Plant D V and Abel S 2023 Thin-film BTO-based modulators enabling 200 Gb/s data rates with sub 1 Vpp drive signal *Optical Fiber Communication Conf.* pp Th4A–2
- [15] Abel S et al 2019 Large Pockels effect in micro- and nanostructured barium titanate integrated on silicon Nat. Mater. 18 42-47
- [16] Li Y, Sun M, Miao T and Chen J 2024 Towards high-performance Pockels effect-based modulators: review and projections Micromachines 15 865
- [17] Zgonik M, Bernasconi P, Duelli M, Schlesser R, Günter P, Garrett M H, Rytz D, Zhu Y and Wu X 1994 Dielectric, elastic, piezoelectric, electro-optic, and elasto-optic tensors of BaTiO₃ crystals *Phys. Rev. B* 50 5941
- [18] Winiger J et al 2024 PLD epitaxial thin-film BaTiO₃ on MgO—dielectric and electro-optic properties Adv. Mater. Interfaces 11 2300665
- [19] Hensling F V E, Braun W, Kim D Y, Majer L N, Smink S, Faeth B D and Mannhart J 2024 State of the art, trends, and opportunities for oxide epitaxy APL Mater. 12 040902
- [20] Zhang Z et al 2025 Preparation and microstructure of BaTiO₃ thin films by RF magnetron sputtering J. Phys.: Conf. Ser. 2961 012003
- [21] Posadas A B et al 2021 Thick BaTiO₃ epitaxial films integrated on Si by RF sputtering for electro-optic modulators in Si photonics ACS Appl. Mater. Interfaces 13 51230–44
- [22] Al Meselmene N, Nemati A, Pan J S, Yuanda L, Dogheche K, Remiens D, Dogheche E and Teng J 2024 Growth and characterization of perovskite BaTiO₃ thin film for optics and photonics applications *Proc. SPIE* 13116 1311602
- [23] Baniecki J D, Ishii M, Shioga T, Kurihara K and Miyahara S 2006 Surface core-level shifts of strontium observed in photoemission of barium strontium titanate thin films Appl. Phys. Lett. 89 162908
- [24] Wegmann M, Watson L and Hendry A 2004 XPS analysis of submicrometer barium titanate powder J. Am. Ceram. Soc. 87 371–7
- [25] Nayak S, Sahoo B, Chaki T K and Khastgir D 2014 Facile preparation of uniform barium titanate (BaTiO₃) multipods with high permittivity: impedance and temperature dependent dielectric behavior RSC Adv. 4 1212–24
- [26] Nasser S A 2000 x-ray photoelectron spectroscopy study on the composition and structure of BaTiO3 thin films deposited on silicon *Appl. Surf. Sci.* 157 14–22
- [27] Fuenzalida V M, Pilleux M E and Eisele I 1999 Adsorbed water on hydrothermal BaTiO₃ films: work function measurements Vacuum 55 81–83
- [28] Awan I T, Lozano G, Pereira-da-silva M A, Romano R A, Rivera V A G, Ferreira S O and Marega E 2020 Understanding the electronic properties of BaTiO₃ and Er³⁺ doped BaTiO₃ films through confocal scanning microscopy and XPS: the role of oxygen vacancies *Phys. Chem. Chem. Phys.* 22 15022–34
- [29] Clabel H J L et al 2015 Near-infrared light emission of Er³⁺-doped zirconium oxide thin films: an optical, structural and XPS study I. Alloys Compd. 619 800–6
- [30] Maneeshya L V, Thomas P V and Joy K 2015 Effects of site substitutions and concentration on the structural, optical and visible photoluminescence properties of Er doped BaTiO₃ thin films prepared by RF magnetron sputtering Opt. Mater. 46 304–9
- [31] Evangelou E K, Konofaos N, Aslanoglou X, Kennou S and Thomas C B 2001 Characterization of BaTiO₃ thin films on p-Si Mater. Sci. Semicond. Process. 4 305–7
- [32] García T, Bartolo-Pérez P, De Posada E, Peña J L and Villagrán-Muniz M 2006 Studies of pulsed laser deposition processes of BaTiO₃ thin films Surf. Coat. Technol. 201 3621—4
- [33] Yu Q, Liu D, Wang R, Feng Z, Zuo Z, Qin S, Liu H and Xu X 2012 The dielectric and photochromic properties of defect-rich BaTiO₃ microcrystallites synthesized from Ti₂O₃ Mater. Sci. Eng. 177 639–44
- [34] Zhang X, Qin J, Xue Y, Yu P, Zhang B, Wang L and Liu R 2014 Effect of aspect ratio and surface defects on the photocatalytic activity of ZnO nanorods Sci. Rep. 4 4596
- [35] Hauser A J et al 2012 Fully ordered Sr₂CrReO₆ epitaxial films: a high-temperature ferrimagnetic semiconductor Phys. Rev. B 85 161201
- [36] Du C, Adur R, Wang H, Hauser A J, Yang F and Hammel P C 2013 Control of magnetocrystalline anisotropy by epitaxial strain in double perovskite Sr₂FeMoO₆ films *Phys. Rev. Lett.* **110** 147204
- [37] Esser B D, Hauser A J, Williams R E A, Allen L J, Woodward P M, Yang F Y and McComb D W 2016 Quantitative STEM imaging of order–disorder phenomena in double perovskite thin films *Phys. Rev. Lett.* 117 176101
- [38] Cheng Y, Cogulu E, Resnick R D, Michel J J, Statuto N N, Kent A D and Yang F 2022 Third harmonic characterization of antiferromagnetic heterostructures *Nat. Commun.* 13 3659
- [39] Lee A J, Brangham J T, Cheng Y, White S P, Ruane W T, Esser B D, McComb D W, Hammel P C and Yang F 2017 Metallic ferromagnetic films with magnetic damping under 1.4×10^{-3} Nat. Commun. 8 234

- [40] Nelson R L, Griffin B G, Brown D P, McKeown S and Stenger V 2019 Barium titanate electro-optic modulators 2019 IEEE Avionics and Vehicle Fiber-Optics and Photonics Conf. (AVFOP) pp 1–2
- [41] Kormondy K J et al 2017 Microstructure and ferroelectricity of BaTiO₃ thin films on Si for integrated photonics Nanotechnology 28 075706
- [42] Posadas A B, Stenger V E, DeFouw J D, Warner J H and Demkov A A 2023 RF-sputtered Z-cut electro-optic barium titanate modulator on silicon photonic platform *J. Appl. Phys.* **134** 073101
- [43] Liu J M 2022 Nonlinear Photonics Nonlinear Photonics 1st edn (Cambridge University Press) ch 11, sec 11.4.3